European Journal of
Mineralogy
Open Access

Micro- to nano-sized solid inclusions in magnetite record skarn reactions

Igor González-Pérez[1], José María González-Jiménez[2], Lola Yesares[3], Antonio Acosta-Vigil[2], Jordi Llopís[1], and Fernando Gervilla[1,2]

[1]Departamento de Mineralogía y Petrología, Facultad de Ciencias, Universidad de Granada,
Avda. Fuentenueva s/n, 18002 Granada, Spain
[2]Instituto Andaluz de Ciencias de la Tierra (IACT), CSIC-UGR, Avda. de las Palmeras 4,
18100 Armilla, Granada, Spain
[3]Departamento de Mineralogía y Petrología, Facultad de Ciencias Geológicas, Universidad Complutense de
Madrid, C/ Jose Antonio Novais,12, Ciudad Universitaria, 28040 Madrid, Spain

Correspondence: Igor González-Pérez (igorgonzpe@ugr.es)

Abstract. Magnetite is a widespread ore mineral in skarn systems and usually hosts a wide variety of inclusions. Micro- to nano-sized solid inclusions in magnetite are unique tools to track the evolutionary processes of its host mineral and, subsequently, to constrain the timing of the mineralization event. In this study, we characterize micro- to nano-sized solid inclusions in magnetite from the La Víbora magnesian skarn (Málaga, Spain) using scanning electron microscopy (SEM) and transmission electron microscopy (TEM). TEM energy-dispersive X-ray spectrometry (EDS) analyses and compositional mapping expose two types of nano-inclusions oriented along the (111) of magnetite: type 1 includes dolomite, spinel, and Mg–Fe–Al silicate, and type 2 is made up of Mg–Fe–Al silicates enveloping the Mg-bearing amorphous silica phase. High-resolution transmission electron microscopy (HRTEM), selected-area electron diffraction (SAED), and fast Fourier transform (FFT) patterns reveal that the majority of the solid inclusions display non-oriented matrices compared to the host magnetite, precluding the possibility of sub-solidus processes. Instead, these inclusions are thought to preserve skarn mineral assemblages that were entrapped during the growth of magnetite. However, the local supersaturation of fluids trapped in the boundary layer of crystallizing magnetite is evidenced by coherent lattice orientation of precipitated and host magnetite and by the occurrence of an Mg-bearing amorphous silica phase. Our findings reveal that skarn reactions observed at field and microscopic scales are also recorded in nano-sized inclusions within magnetite. These observations underscore the significance of micro- to nano-scale solid inclusions in magnetite to decipher overprinted skarn reactions as well as constraining the timing of Fe mineralization events in skarns.

1 Introduction

Skarn deposits represent one of the most prevalent ore deposits, distributed widely across the Earth's crust (e.g., Einaudi et al., 1981; Meinert et al., 2005; Chang et al., 2019; Kuşcu, 2019). These deposits contain resources of several base metals (Fe, Cu, Pb, Zn, W, Mo, Sn; e.g., Zhang et al., 2013, 2014; Calvo et al., 2013; Jansson and Allen, 2015; Zhao et al., 2017; Lefebvre et al., 2019; Xie et al., 2021; Soloviev et al., 2021) and precious metals (Au, Ag; e.g., Cepedal et al., 2000; Mao et al., 2017; Xie et al., 2019; Guo

et al., 2023) as well as other elements of high-tech and industrial interest (rare earth elements (REE), U, B; e.g., Marincea and Dumitraş, 2019; Fitros et al., 2020; Zheng et al., 2020). Magnetite is widespread in skarn deposits across various geological settings (Einaudi et al., 1981; Meinert et al., 2005), so it has been proposed as a useful petrogenetic indicator based on its trace element distribution (e.g., Dupuis and Beaudoin, 2011; Dare et al., 2014; Nadoll et al., 2014; Knipping et al., 2015; Huang et al., 2019; Canil and Lacourse, 2020; Chen et al., 2020). The presence of micro-

to nano-sized inclusions in magnetite may strongly affect its trace element distribution (e.g., Yin et al., 2019; Deditius et al., 2018; Huang and Beaudoin, 2021), making textural characterization a decisive preliminary step for obtaining petrogenetic insights from magnetite. However, the significance of micro- to nano-sized inclusions in magnetite extends beyond geochemical considerations, particularly when evidence of primordial geological and/or mineralogical context is overridden. Thus, micro- to nano-sized inclusions in magnetite are increasingly being used to unravel the geological setting of ore formation, to characterize distinct alteration events, and to constrain the physicochemical conditions of the ore system. For instance, the oxy-exsolution of ilmenite and spinel in magnetite from the Kovdor phoscorite–carbonatite complex, Russia, was employed to constrain temperature and oxygen fugacity of coexisting magnetite and its exsolution products (Ivanyuk et al., 2017). Amphibole and pyroxene nano-inclusions in magnetite from the Los Colorados iron oxide–copper–gold (IOCG) deposit (Deditius et al., 2018) and from the Sossego IOCG deposit (Huang and Beaudoin, 2021) provide evidence for discriminate magnetite origin. The mineral assemblage of inclusions in magnetite, including silicates (i.e., actinolite, diopside, and epidote) or oxides (i.e., ilmenite and spinel), has been proposed to distinguish between IOCGs sensu stricto and iron oxide–apatite (IOA) deposits (Ciobanu et al., 2019). The latter authors also proposed the use of actinolite, diopside, and epidote nano-inclusions to characterize alteration stages in the Olympic Dam, South Australia. More recently, the volumetric percentage of exsolved spinel in magnetite from the San Manuel skarn was used to approximate the maximum temperature of magnetite mineralization (González-Pérez et al., 2022).

Despite the numerous studies investigating micro- to nano-inclusions in magnetite principally in hydrothermal systems, research characterizing mineral assemblages within micro- to nano-sized inclusions in magnetite to track overprinted mineral reactions in magnesian skarn ore-forming systems remains limited. This research focuses on the micro- to nano-scale characterization of solid inclusions within magnetite from the La Víbora magnesian skarn (Málaga Province, SW Spain). This magnesian skarn is hosted within dolomitic marbles of the contact aureole resulting from the crustal emplacement of the Ronda peridotites. Typical zoning of magnesian skarns is observed, featuring distinct mineralogical zones including the (1) forsterite, (2) diopside, and (3) periclase zones. Notably, micro- to nano-sized solid inclusions are systematically oriented along the (111) of magnetite and are exclusively found in coarse magnetite cores from the periclase zone. This study highlights the significance of micro- to nano-scale inclusions in magnetite as a tool for deciphering overprinted skarn reactions and constraining the timing of the mineralization.

2　Geological setting

The La Víbora magnesian skarn is located in the northern sector of the Sierra Bermeja, approximately 15 km southeast of the city of Ronda in southern Spain (Fig. 1). This area belongs to the Betic Cordillera, which corresponds to the northern portion of the Betic–Rif orogenic belt in the westernmost part of the Mediterranean region (e.g., Platt et al., 2013). The geology of the Betic Cordillera is subdivided into three main geological domains: external zones, internal zones, and the flysch, the latter sandwiched between the other two domains. The external zones are located to the north of the Betic Cordillera and correspond to the sedimentary cover deposited during the Mesozoic to Cenozoic on the Iberian foreland. The internal zones correspond to sediments deposited between the Iberia and Africa plates during Paleozoic to Mesozoic times that were subsequently metamorphosed and stacked during the Alpine orogeny. The internal zones are made up of three nappe complexes: the Nevado–Filábride Complex at the bottom, the Alpujárride Complex in the middle, and the Maláguide Complex at the top of the tectonic sequence (Egeler and Simon, 1969). The flysch is composed of turbiditic sediments deposited from the Cretaceous to Miocene in deep marine basins located in the Alboran Sea (Vissers et al., 1995).

The La Víbora skarn belongs to the Alpujárride Complex, which in the studied area comprises the Blanca unit at the bottom and the Jubrique unit at the top (Navarro-Vilá and Tubía, 1983; Tubía and Cuevas, 1986; Tubía et al., 2013). The Blanca unit consists of a crustal sequence composed of Upper Triassic dolomitic marbles lying on high-grade metapelites and migmatites (Tubía et al., 1997; Sánchez-Rodríguez and Gebauer, 2000). Migmatites are interpreted as the product of the partial melting of former metapelitic rocks during the hot emplacement of the mantle peridotites (1100–800 °C and 1.4–1.1 GPa; Tubía et al., 1997, 2013; Cuevas et al., 2006; Esteban et al., 2008). The Blanca unit is overthrust by the Ronda peridotites (i.e., mainly Ronda, Ojén, and Carratraca massifs), which mostly consist of lherzolites and harzburgites with minor amounts of dunite as well as different types of pyroxenite layers, locally intruded by leucocratic dikes (Obata, 1980; Van der Wal and Vissers, 1993, 1996; Garrido and Bodinier, 1999; Acosta-Vigil et al., 2014). These peridotites are exposures of a Proterozoic (1.2–1.8 Ga) subcontinental lithospheric mantle (SCLM) (Reisberg and Lorand, 1995; Marchesi et al., 2010; González-Jiménez et al., 2013a, b) finally emplaced in the crust during the late Oligocene to Early Miocene (e.g., Esteban et al., 2004, 2007, 2010; Precigout et al., 2007; González-Jiménez et al., 2017), although a recent debate involving a pre-Alpine age for peridotite emplacement is becoming controversial (e.g., Acosta-Vigil et al., 2014; Barich et al., 2014; Sanz de Galdeano and Ruiz-Cruz, 2016; Sanz de Galdeano, 2023; Díaz-Alvarado et al., 2024; Sánchez-Navas et al., 2024). The peridotite emplacement has been related to the development of a back-arc
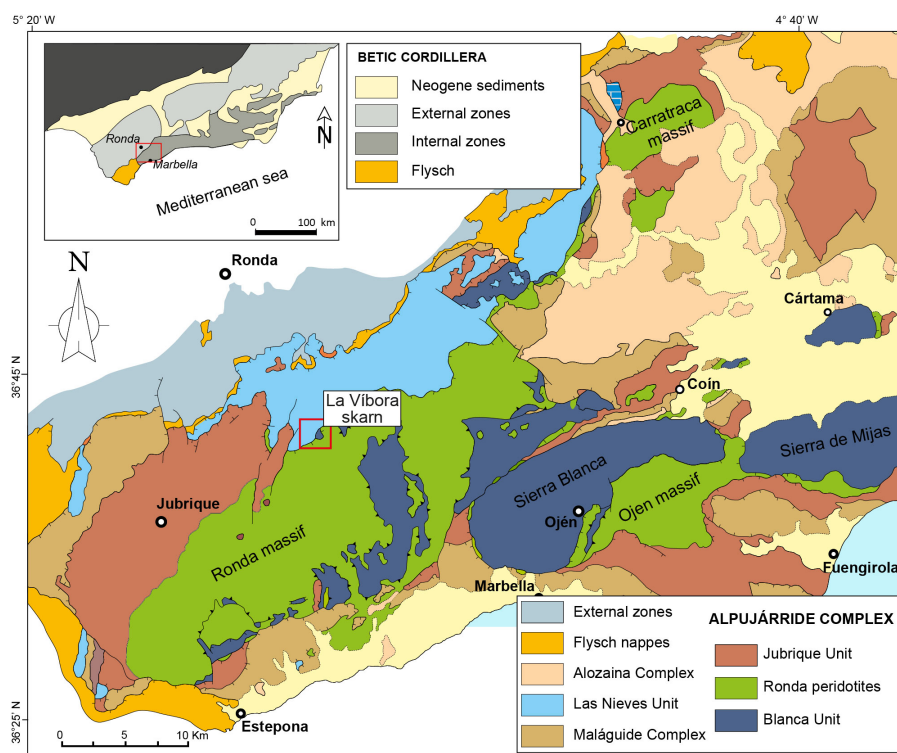
Figure 1. Geological map of the western zone of the Betic Cordillera, southern Spain. Modified from Gervilla et al. (2019).

basin behind the Betic–Rif orogenic wedge (Garrido et al., 2011; Marchesi et al., 2012; Hidas et al., 2013, 2015). The peridotites are overlain by a thick (up to 7 km) sequence of metapelitic rocks showing a decreasing metamorphic grade outwards from the contact with the peridotites (i.e., Jubrique unit) (Balanyá et al., 1997; Tubía et al., 1997; Platt et al., 2013). These rocks correspond to vestiges of a pre-Mesozoic continental crust that also experienced substantial thinning during the Late Oligocene/Early Miocene.

In the studied area, the Ronda peridotite unit tectonically overlies the Las Nieves unit, which is formed by ca. 1.5 km thick Mesozoic to Cenozoic platform deposits, including limestones, dolomites, and marls. It is considered a non-metamorphic and slightly deformed unit although it is intensely metamorphosed towards the contact with the Ronda peridotites (Mazzoli and Martínez-Algarra, 2011; Sanz de Galdeano, 2023). The tectonic contact at the base of the peridotites with the footwall rocks of the Las Nieves unit consists of an up to 200 m thickness shear zone made up of mylonite that locally embeds blocks of the Blanca unit.

3 Samples and analytical methods

A total of 10 rock samples were picked from different zones of the skarn, including dolomitic marble. Considering that the skarn outcrop is in a vertical area of ~40 m thickness, we consider such a number of samples representative enough

for the skarn. Thin sections of ~30 μm thickness were investigated using a ZEISS JENAPOL optical microscope in transmitted and reflected light from the Departamento de Mineralogía y Petrología at the Universidad de Granada.

Analysis of the in situ chemical composition of minerals was conducted using electron probe micro-analysis (EPMA) using a JEOL JXA-8230 analyzer equipped with wavelength-dispersive X-ray (WDX) detectors at Servicios Científico-Técnicos, Universidad de Barcelona. The accelerating voltage was 20 kV, the beam current was 20 nA, and the beam diameter was 5 μm. Analytical procedures of EPMA of silicates and oxides are provided in Tables S1 and S2 (Supplement 1). Both peak and background counting times were measured over 10 s. Data reduction followed the phi–rho–z procedure proposed by Pouchou and Pichoir (1991), whereas Fe^{2+} and Fe^{3+} were calculated by charge balance according to Droop (1987).

Textural characterization of minerals was carried out by means of a Phenom XL scanning electron microscope operating in backscattered electron (BSE) mode, whereas semi-quantitative chemical maps were made by energy-dispersive X-ray spectroscopy (EDS) at the Departamento de Mineralogía y Petrología at the Universidad de Granada, Spain. The accelerating voltage was 15 keV and the beam current was 1 nA for a sufficient number of counts for each EDS analysis. The Phenom software automatically carries ZAF corrections to reduce absorption and fluorescence effects.

The Phenom algorithm uses the extended algorithm of Pouchou and Pichoir (1993) to reduce the effect of changes on X-ray transmission through the interaction volume as a function of the accelerating voltage and the matrix it penetrates.

Two thin foils crosscutting nano-inclusions in magnetite from sample V-10 were extracted using focused ion beam scanning electron microscopy (FIB–SEM) at the Laboratorio de Microscopías Avanzadas (LMA) at the Instituto de Nanociencia y Materiales de Aragón (INMA) – Universidad de Zaragoza, Spain. Thin-foil preparation for transmission electron microscopy (TEM) was performed using a dual-beam FEI Thermo Fisher Scientific Helios 650. The selected regions of interest were first covered by a thin strip (~ 300 nm) of C and Pt for protection during milling, polishing, and extraction. The bulk material was first removed on both sides of the lamella by rough Ga^+ ion milling with a voltage of 30 kV at a current of 2.5 nA, and the subsequent polishing was performed with a voltage of 30 kV at a current of 0.23 nA. The thin foils were polished with Ga^+ ion milling to achieve electron transparency, which was monitored by an Everhart–Thornley secondary electron (SE) detector. After achieving the electron transparency, the thin foils were rapidly polished using low energy of 5 kV at a current of 10 pA to reduce the amorphization until a final thickness of ~ 90 nm was attained. Subsequently, the thin foils were undercut with a 30 kV at 2.5 nA current, lifted out, and transferred from the sample to a TEM grid using an OmniProbe nano-manipulator.

A Thermo Fisher Scientific Talos F200X and an FEI Titan G2 transmission electron microscope, both equipped with X-FEG field emission guns, were used in combination to analyze the thin foils at the Centro de Instrumentacíon Científica (CIC) of the Universidad de Granada, Spain. The Talos and FEI Titan G2 microscopes included four energy-dispersive X-ray (EDX) detectors and one high-angle annular dark-field (HAADF) detector, each one operating in scanning transmission electron microscopy (STEM) mode. Selected areas within the thin foils were imaged by the FEI Titan G2 microscope using HAADF-STEM to obtain high-Z-contrast images as well as high-resolution TEM (HRTEM) images. The fast Fourier transform (FFT) method is applied to HRTEM images to obtain FFT diffraction patterns and thus see the orientation of the crystal lattice and its spacings. All these images were treated using the DigitalMicrograph® software (Version 1.71.38). Selected-area electron diffraction (SAED) was also performed. The FEI Titan G2 was running at 300 kV working conditions while HRTEM images were acquired using a Gatan CCD camera. The Thermo Fisher Scientific Talos F200X was employed for single-spot analytical electron microscopy (AEM) analysis and to acquire compositional elemental maps of the sample using an accelerating voltage of 200 kV and image drift correction. Elemental maps were also processed using the Velox® software.
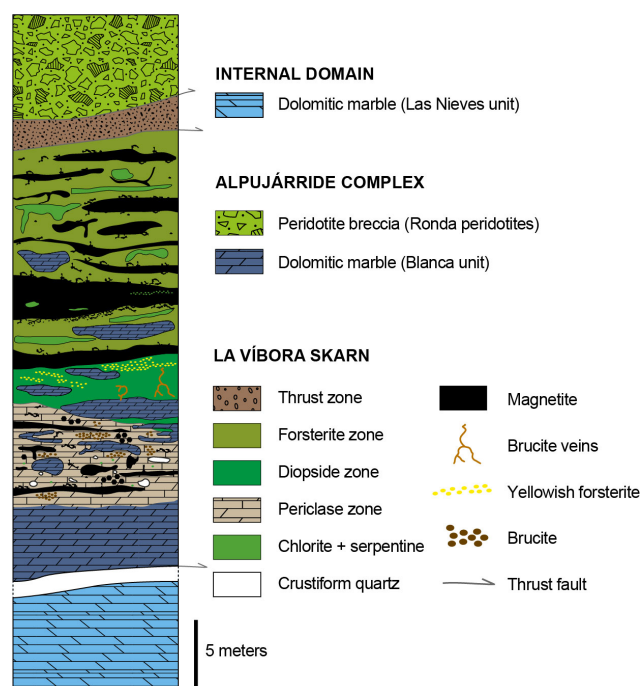

Figure 2. Schematic stratigraphic column of the La Víbora skarn.

4　Results

4.1　Petrography of the La Víbora skarn

4.1.1　Skarn zones and petrography

The La Víbora skarn is hosted in dolomitic marbles from a dismembered block of the Blanca unit (~ 20 m thick), which is now embedded in a shear zone at the northern contact of the Ronda peridotites with carbonates of the Las Nieves unit (Fig. 1). The Ronda peridotites overthrust in northwestern-direction marbles of the Las Nieves unit, which are extensively deformed forming an inverse fold at the contact with the ultramafic rocks (see Mazzoli and Martínez-Algarra, 2011). For the sake of clarity, a schematic column of the skarn is shown in Fig. 2. In the area, the Ronda peridotites are exposed in the westernmost part of the area in the form of breccia, which is made up of heterometric (up to 20 cm), rounded to angular blocks (Fig. 3a–b) of serpentinized forsterite embedded in a mixture of serpentine and minor brucite (Fig. 4a).

The mineralization in the skarn is made up of magnetite, whereas gangue minerals include dolomite, forsterite, diopside, calcite, periclase, brucite, serpentine-group minerals, and chlorite, as well as minor graphite, amorphous silica, and amphibole. According to the dominant gangue mineral, three different zones are distinguished (Fig. 2).

1. *Forsterite zone.* This occupies the westernmost part of the skarn, at the contact with the thrust zone, which separates the skarn from the brecciated Ronda peridotites

(Fig. 3a, c). This zone consists of dolomitic marble partially replaced by serpentinized forsterite, calcite, and varying amounts of chlorite. Pods and veins of massive to semi-massive magnetite are widespread in this zone (Fig. 3c), where magnetite is interstitial to partially serpentinized forsterite grains, the latter being up to 1 mm in size (Fig. 4b).

2. *Diopside zone.* This is situated in the intermediate part of the skarn, where dolomitic marble is partially replaced along fringes and/or fractures (Fig. 3d–e). Diopside occurs as euhedral to subhedral prismatic grains that are up to 2 mm in size replacing forsterite (Fig. 4c), and it is locally replaced by minute, euhedral crystals of amphibole. Diopside also occurs as monomineralic, granoblastic masses of prismatic crystals of up to 1 mm, locally crosscut by brucite veins (Fig. 4d). Two types of serpentine minerals are observed in this zone. Srp-1 is yellowish and replaces forsterite, whereas Srp-2 is white-colored and forms magnetite-bearing veins crosscutting and replacing both forsterite and diopside; the latter is also locally replaced by chlorite (Fig. 4c). Notably, magnetite is nearly absent in this zone, except for trails of microcrystalline magnetite disposed throughout the serpentine veins replacing forsterite and diopside (Fig. 4c).

3. *Periclase zone.* This is located at the easternmost part of the skarn in contact with unaltered dolomitic marble. In this zone, brucitized periclase grains of up to 1 mm in size are disseminated along with calcite, magnetite, and minor chlorite (Fig. 4e–g). Remnants of unaltered dolomitic marble remain perceptible, exhibiting acicular crystals of graphite as well as dismembered forsterite grains (Fig. 4h). Voids and fractures are filled with minute calcite-comb crystals growing outwards from fracture walls, followed by a parallel controlled, finely banded, crustiform Mg-bearing silica amorphous phase. The innermost regions of fractures are unfilled (Fig. 4h–i). In this area, both granular or semi-massive magnetite bands and disseminations of magnetite are observed (Fig. 4e, f).

4.1.2 Texture of ore minerals

Magnetite is ubiquitously distributed across the skarn, except for the diopside zone, which is restricted to serpentine veins. The mineralization forms heterometric pods and bands of up to 0.5 m thickness, made up of variably textured magnetite. Three predominant magnetite ore textures characterize the mineralization.

1. *Massive to semi-massive.* This texture is prevalent throughout the forsterite zone. Massive-textured ore usually forms the core of the pods and is made up of granoblastic magnetite of up to 0.4 mm in size with sharp and irregular contacts and frequently forming 120° triple junctions (Figs. 4j and 5a). Semi-massive magnetite is generally associated with the external zones of magnetite pods and veins. It comprises variably sized granoblastic magnetite of up to ~ 0.2 mm in size and interstitial to serpentinized forsterite (Fig. 4b, k). Semi-massive magnetite boundaries are sharp and range from irregular and/or corroded to curved 120° triple junctions (Fig. 5b). Inclusions of serpentinized forsterite are widespread in both massive and semi-massive magnetite (Figs. 4j, k and 5a, b).

2. *Coarse granular.* This texture is composed of coarse magnetite (> 2 mm) forming discrete grains or massive bands with sawtooth-shaped boundaries (Fig. 4l) or occurring as discrete grains embedded within a matrix of massive to semi-massive magnetite (Fig. 4k). Notably, coarse granular magnetite within the periclase zone showcases solid inclusions conformably oriented with (111) planes of magnetite in its cores (Fig. 5c–d). Cracks crosscutting coarse granular magnetite often contain calcite, dolomite, and chlorite (Fig. 5d).

3. *Disseminated magnetite.* This texture is found as dispersed magnetite grains ranging from 0.25 to 0.5 mm in size. Disseminated magnetite occurs embedded within the matrix of the different skarn zones (Fig. 4e–g) or as trails of tiny magnetite associated with serpentinization in the diopside zone (Fig. 4c).

4.2 Chemical composition of minerals

Forsterite, diopside, and serpentine were analyzed by EPMA ($n = 29$). The whole dataset with EPMA results of silicates is included in Table S3 (Supplement 1). Overall, forsterite ($n = 9$) is MgO-rich (52.68 wt %–57.59 wt %) and has relatively elevated Fe values (FeO$_{tot}$ = 2.86 wt %–6.29 wt %), whereas SiO$_2$ ranges from 38.43 wt %–42.23 wt %. MnO concentration ranges from 0.04 wt %–0.19 wt %. The Mg-rich nature of forsterite is evident in its end-member percentage of Fo$_{94-97}$–Fa$_{3-6}$. Srp-1 ($n = 8$) is yellow Fe-rich serpentine replacing forsterite from the diopside zone (Fig. 4c). It has low MgO (33.71 wt %–37.34 wt %) and SiO$_2$ (38.46 wt %–39.94 wt %) but elevated Fe (FeO$_{tot}$ = 7.39 wt %–10.18 wt %) values. NiO is systematically < 0.11 wt %. On the other hand, Srp-2 ($n = 6$) is a vein-like Fe-rich serpentine with higher MgO (42.07 wt %–41.15 wt %) and SiO$_2$ (39.56 wt %–41.20 wt %) than Srp-1 but lower Fe (FeO$_{tot}$ = 2.09 wt %–3.91 wt %) and NiO (0.08 wt % to 0.32 wt %). MnO is below 0.04 wt % in both types of serpentine. Diopside ($n = 12$) is relatively homogeneous in terms of SiO$_2$ (50.49 wt %–55.03 wt %), MgO (16.90 wt %–18.75 wt %), and CaO (23.29 wt %–26.19 wt %), whereas FeO (0.51 wt %–4.34 wt %) and Al$_2$O$_3$
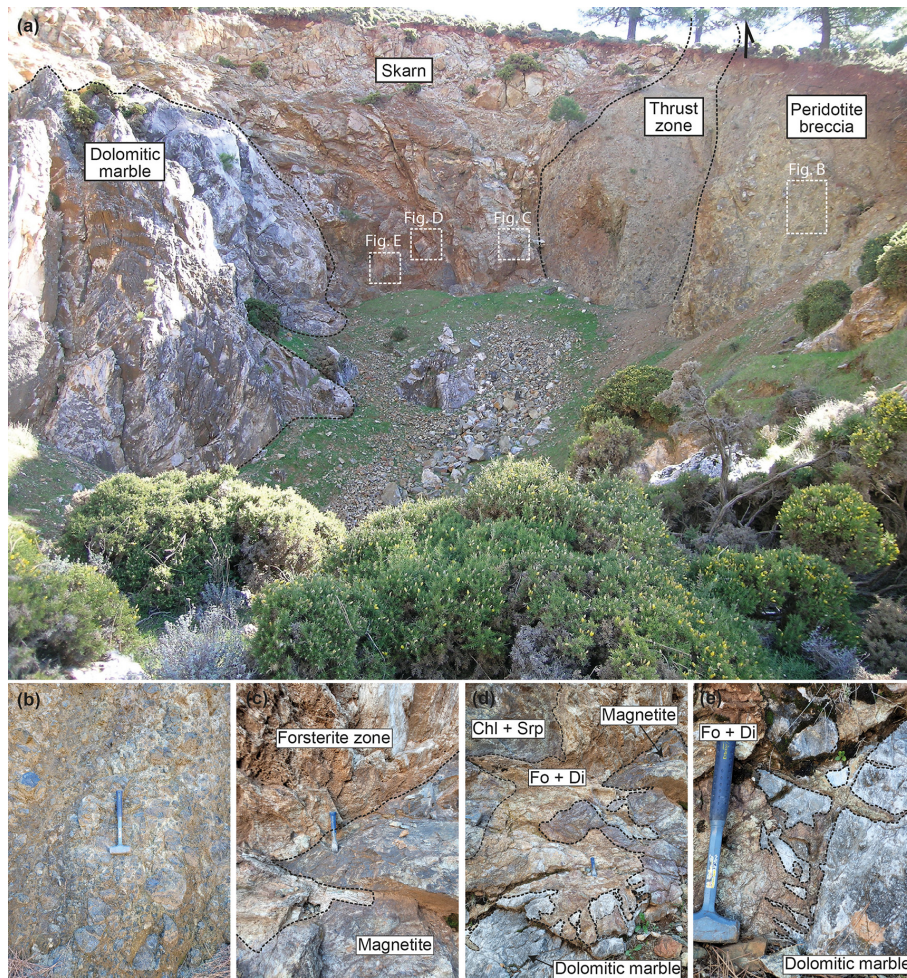
Figure 3. Field images of the La Víbora skarn. **(a)** Overview of the skarn area. **(b)** Peridotite breccia. **(c)** Pod of magnetite from the forsterite zone. **(d)** Partially replaced dolomitic marble along fringes of forsterite and diopside, as well as irregular mass of magnetite. **(e)** Forsterite and diopside replacing dolomitic marble along fractures. Fo: forsterite; Di: diopside; Chl: chlorite; Srp: serpentine.

(0.04 wt %–2.39 wt %) values show a wider range of concentrations.

A total of 90 analyses were carried out in magnetite by means of EPMA. Magnetite with variable Mg contents is the only ore mineral in the La Víbora skarn. Overall, a consistent trend of Mg decrease is observed towards the boundaries of magnetite grains in all textures throughout the skarn. Despite the diversity in texture, the composition of magnetite is very homogeneous, except for granular magnetite ($n = 31$), which exhibits higher $Mg\# = [Mg / (Mg+Fe^{2+})]$ ratios ($Mg\# = 0.25$–0.42) compared to semi-massive ($n = 36$; $Mg\# = 0.18$–0.29) and massive ($n = 23$; $Mg\# = 0.21$–0.23) magnetite. The Al_2O_3 content is low in massive magnetite ($Al_2O_3 = 0.01$ wt %–0.06 wt %), whereas in semi-massive magnetite, the Al_2O_3 content depends on the skarn zone of the analyzed magnetite. Thus, semi-massive magnetite from the forsterite zone has $Al_2O_3 = 0.58$ wt %–1.61 wt %, whereas that of the periclase zone ranges between 0.08 wt %

and 0.073 wt % Al_2O_3. Coarse granular magnetite has elevated Al_2O_3 contents ($Al_2O_3 = 0.23$ wt %–1.49 wt %), especially in a coarse granular magnetite grain embedded within semi-massive magnetite ($Al_2O_3 = 0.89$ wt %–2.11 wt %). The minor element composition of magnetite proves to be uniform, displaying no significant chemical variations concerning the skarn zone or the type of texture. SiO_2 reaches up to 1.11 wt %, whereas Al_2O_3 ranges between 0.08 wt %–2.11 wt %. The other minor elements yield values below 0.25 wt % (Supplement 1; Table S4).

4.3   Solid inclusions in magnetite

The solid inclusions in magnetite are variable in mineralogy, size, and distribution across the skarn zones. There are two types of inclusions based on their size and textural relationships with magnetite:

Micro-scale, non-oriented inclusions of forsterite and calcite and dolomite. Forsterite inclusions are predominantly
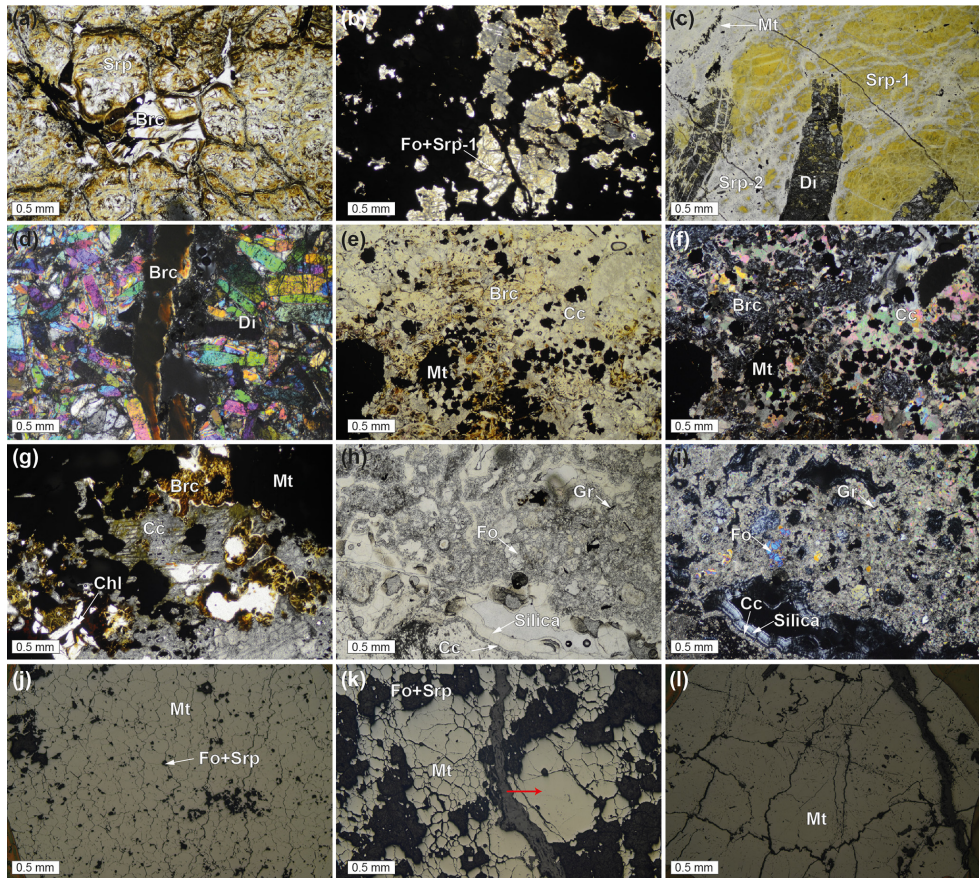
Figure 4. Photomicrographs of the different zones of the skarn. **(a)** Transmitted plane-polarized light of serpentinized forsterite grains and brucite masses from the peridotite breccia. **(b)** Transmitted plane-polarized light from the forsterite zone showing masses of magnetite interstitial to partially serpentinized forsterite. **(c)** Transmitted plane-polarized light displaying prismatic diopside crystals replacing forsterite and serpentinization of both silicates. Note tiny magnetite grains associated with serpentinization in the upper-left part of the photomicrograph. **(d)** Transmitted cross-polarized light of granoblastic masses of diopside from the diopside zone crosscut by a brucite vein. **(e)** Transmitted plane-polarized and **(f)** cross-polarized light photomicrographs showing the general aspect of the periclase zone with disseminated magnetite. **(g)** Transmitted plane-polarized light photomicrograph of calcite, brucite, and tabular-like chlorite crystals coexisting with magnetite from the periclase zone. **(h)** Transmitted plane-polarized and **(i)** cross-polarized photomicrographs showing partially replaced dolomitic marble. Note the presence of isolated forsterite and acicular graphite. Voids are filled with comb carbonate crystals at the margins and banded, crustiform silica in the inner parts. Reflected-light images showing the different textures of magnetite: **(j)** massive, **(k)** semi-massive, and **(l)** coarse granular magnetite. A coarse magnetite grain embedded within the semi-massive magnetite is marked with a red arrow **(k)**. Srp: serpentine; Brc: brucite; Fo: forsterite; Di: diopside; Mt: magnetite; Chl: chlorite; Cc: calcite; Gr: graphite.
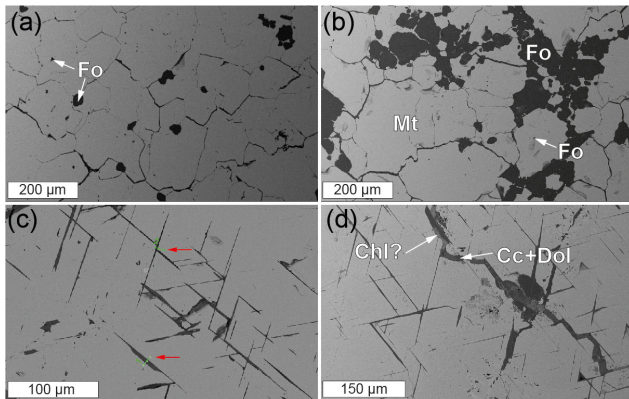
found in massive and semi-massive magnetite from the forsterite zone. They exhibit rounded shapes with sizes varying from $\sim 10\,\mu m$ to $\sim 0.1\,mm$ (Fig. 5a, b). On the other hand, coarse granular magnetite hosts composite inclusions made up of calcite and dolomite with irregular shapes of up to $80\,\mu m$ (Fig. 6a–c), which may locally grade into Si-rich filled fractures and/or discrete inclusions completely sealed by magnetite (Fig. 6d).

Micro- to nano-sized inclusions oriented along the {111} of magnetite (Fig. 5c–d). They are made up of dolomite; nano-inclusions of spinel, chlorite, and likely serpentine; and an Mg-bearing amorphous silica phase. These inclusions are exclusively found in cores of coarse granular magnetite from

the periclase zone (sample V-10). Based on backscattered electron (BSE) imaging and SEM–EDS semi-quantitative compositional maps (Fig. 6), these oriented nano-inclusions have been categorized into two different sub-groups.

(2a) Type 1 inclusions (white squares in Fig. 6). These are Ca- and Mg-rich, with variable Si. They are small ($< 5\,\mu m$) and display elongated shapes with sharp boundaries with host magnetite, although often irregular, curved boundaries are also observed.

(2b) Type 2 inclusions (yellow squares in Fig. 6). These are Si-rich, with variable Mg and no Ca, and display sizes similar to type 1 inclusions but are slightly thinner. They are

Figure 5. Backscattered electron images of different types of inclusions in magnetite. **(a, b)** Non-oriented forsterite inclusions in **(a)** massive and **(b)** semi-massive magnetite. **(c, d)** Needle-like oriented inclusions along {111} of magnetite. Red arrows in **(c)** highlight the location of FIB thin foils. Note the presence of late veins crosscutting coarse granular magnetite, filled with calcite, dolomite, and likely chlorite. Fo: forsterite; Mt: magnetite; Chl: chlorite; Cc: calcite; Dol: dolomite.

needle-shaped inclusions with sharp and straight boundaries with host magnetite.

The FIB thin foil crosscutting a type 1 inclusion was obtained from sample V-10 (Fig. 7a). High-angle annular dark-field scanning transmission electron microscopy (HAADF-STEM) imaging reveals the presence of various constituents (Fig. 7b) that display sharp compositional boundaries in relative concentrations of Mg, Ca, Al, Fe, and Si (Fig. 7c, j, k). Through comprehensive analyses including TEM–EDS maps, selected-area electron diffraction (SAED), HRTEM, and corresponding FFT patterns, the inclusions were identified as follows: (1) dolomite; (2) spinel; and (3) Fe-rich and Fe-poor intergrowths of Mg-, Si-, and Al-bearing nano-inclusions, most likely intermediate members of the clinochlore–chamosite solid solution.

Dolomite dominates in the central region of the FIB thin foil (Fig. 7b–c). SAED analysis yielded d spacing of 2.88, 2.66, and 1.78 Å corresponding to (104), (006), and (116) of dolomite, respectively, consistent with Goldsmith et al. (1961) (Fig. 7d–e). HRTEM imaging shows a sharp boundary between dolomite and host magnetite with nano-domains in dolomite exhibiting multiple orientations relative to the host magnetite (Fig. 7f). Another nearby area was chosen for SAED analysis in spinel (Fig. 7g), which yielded d spacing of 4.63, 2.85, and 2.45 Å, consistent with ($1\bar{1}1$), (220), and (311) of the spinel structure, as reported by Peterson et al. (1991). HRTEM images show a coherent lattice orientation between spinel and host magnetite, characterized by a curved and sharp boundary. However, the SAED and FFT patterns indicate a lattice rotation of approximately 90° to each other (inset in Fig. 7h).

A detailed examination of the left region of the thin foil using HRTEM imaging (Fig. 7i) and TEM–EDS elemental mapping (Fig. 7j, k) unveiled an intergrowth of Fe-rich and Fe-poor Mg-, Si-, and Al-bearing minerals. It has a laminar habit and displays a sharp compositional boundary with host magnetite and several voids (Fig. 7j–l). The HRTEM imaging in this zone revealed curved crystallographic planes (Fig. 7l). FFT patterns yield d-spacing values of 4.72 (003), 3.53 (004), and 2.58 Å ($20\bar{2}$), corresponding to {h01} for the structure of monoclinic polytype IIb chlorite (Brown and Bailey, 1962). A second set of measured d-spacing values including 4.07 ($\bar{1}12$), 3.82 (022), 3.67 (112), and 3.32 Å (116) (Supplement 2) corresponds to {hk1} values for chamosite nanocrystals (Walker and Bish, 1992).

A second FIB thin foil was performed across a type 2 inclusion from sample V-10 (Fig. 8a). HAADF-STEM and TEM–EDS elemental mapping reveal a composite inclusion comprising a Fe-, Mg-, and Al-bearing silicate of < 500 nm, encapsulating a net-like, Si- and Mg-bearing phase of about 1 µm in thickness (Fig. 8b–d). Through comprehensive analyses including SAED, HRTEM, and corresponding FFT patterns, the nano-inclusions were categorized into (1) intermediate members of the clinochlore–chamosite solid solution and (2) an Mg-bearing amorphous silica phase.

Intergrowths of intermediate members of the clinochlore–chamosite solid solution were observed on both sides of the thin foil, in direct contact with hot magnetite (Fig. 8b). SAED measurements at the contact between magnetite and chlorite (Fig. 8d) yielded d-spacing values of 7.20, 7.05, and 4.74 Å, matching (004), (002), and (003) of monoclinic polytype IIb chlorite (Brown and Bailey, 1962; Lister and Bailey, 1967), as well as 4.83 Å corresponding to the {111} of magnetite (Nakagiri et al., 1986; Bosi et al., 2009) (Fig. 8e). Further SAED, HRTEM imaging, and FFT patterns corroborated these findings, yielding d-spacing values of 4.24 and 2.08 Å (Supplement 2) that fit well with ($1\bar{1}1$) and ($\bar{2}05$) of chamosite (Walker and Bish, 1992). A d-spacing value of 2.08 Å may correspond to (043) of stoichiometric chrysotile (Falini et al., 2004). Despite the potential presence of chrysotile, the Al signal observed in TEM–EDS maps highlighted intermediate members of clinochlore–chamosite as the predominant mineral. As observed in thin foil 1, several voids are observed among clinochlore–chamosite intergrowths (Fig. 8d) Although HRTEM imaging shows coherent lattice orientation between clinochlore–chamosite intergrowths and host magnetite at the very contact (Fig. 8f), a slight misorientation of ∼ 2° is observable in SAED patterns (Fig. 8e). Moreover, the crystallographic planes of clinochlore–chamosite intergrowths curved outwards from the boundary with host magnetite and displayed localized areas with multiple lattice orientations (Fig. 8f).

Clinochlore–chamosite intergrowths were also observed in the right region of thin foil 2, characterized by Fe-richer compositions (Fig. 8g). HRTEM imaging reveals coherent lattice orientation between clinochlore–chamosite intergrowths and
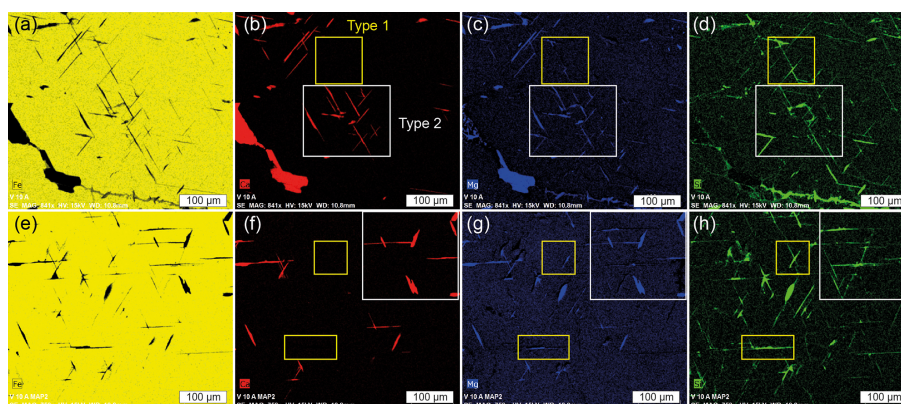
Figure 6. SEM–EDS maps of coarse granular magnetite showing the major element composition of oriented inclusions: **(a, e)** Fe, **(b, f)** Ca, **(c, g)** Mg, and **(d, h)** Si. White squares highlight Ca- and Mg-rich type 1 inclusions, and yellow squares mark Si-rich type 2 inclusions. Non-oriented calcite and dolomite inclusions are displayed at the bottom of SEM–EDS maps in **(a)**–**(d)**.

host magnetite (Fig. 8h). A group of d-spacing values measured in SAED patterns give 4.22 and 2.26 Å, corresponding to $(\bar{1}11)$ and $(\bar{2}04)$, respectively, of chamosite (Walker and Bish, 1992) and 1.72 Å (207) for the structure of monoclinic polytype IIb chlorite (Brown and Bailey, 1962).

The central part of the thin foil comprises a net-like, Si- and Mg-bearing material with several voids. Notably, the SAED pattern obtained from such inclusion evidence an amorphous phase (Fig. 8j–k).

5 Discussion

5.1 Origin of oriented micro- to nano-inclusions in magnetite

Coarse magnetite from La Víbora skarn has nano-inclusions oriented along the (111) of its magnetite host. Such micro- to nano-inclusions comprise dolomite, spinel, intergrowths of intermediate members of clinochlore–chamosite solid solution, and an Mg-bearing amorphous silica phase. Oriented nano-inclusions in magnetite may be interpreted as being due to (1) sub-solidus exsolution from the magnetite host (e.g., Ivanyuk et al., 2017; Deditius et al., 2018); (2) local supersaturation of fluids under non-equilibrium conditions at the boundary layer of crystallizing magnetite, followed by entrapment by the growing magnetite (Watson, 1996; Watson et al., 2011); or (3) relic minerals of the skarn reaction that were mechanically trapped during magnetite growth (e.g., Zhao and Zhou, 2015).

Thin foil 1 is made up of dolomite, spinel, and intermediate members of the clinochlore–chamosite solid solution. TEM–EDS compositional maps reveal variable Fe contents in clinochlore–chamosite intergrowths (Fig. 7j–k). Fe in octahedral sites in chlorite may lead to a distortion of the cell parameters (e.g., Brown and Bailey, 1962). This makes it difficult to accurately link the measured d spacing with either chlorite or chrysotile, as both are common minerals found in magnesian skarns. Based on the Al contents observed in TEM–EDS maps (Figs. 7j and 8c), we suggest that an intermediate member of the clinochlore–chamosite solid solution is the most plausible phase found in the thin foil. Such a hypothesis is supported by a similar mineral assemblage observed in fractures crosscutting magnetite, where chlorite occurs along with dolomite partially replaced by calcite (Fig. 5d). However, the presence of serpentine-group minerals cannot be completely ruled out, as previous studies have demonstrated the existence of Al-bearing serpentine (e.g., Mellini, 1982; O'Hanley and Dyar, 1993). In any case, the presence of chlorite and/or serpentine-group minerals is a typical mineral assemblage of the retrograde stages of magnesian skarns (Aleksandrov, 1998).

Minerals exsolved from magnetite solid solutions during slow cooling involving Fe–Ti–V oxides have been widely documented (Ivanyuk et al., 2017; Ciobanu et al., 2019; Hu et al., 2015; Tan et al., 2016; Huang and Beaudoin, 2019, 2021). This style of sub-solidus state diffusion usually results in spinodal decomposition or nucleation and growth of precipitates from the host mineral (Yund and McCallister, 1970). However, the lack of an epitaxial relation observed between dolomite and the magnetite host (Fig. 7f) does not support solid-state diffusion processes (e.g., Putnis, 2002, 2009; Keller and Ague, 2022). Moreover, the abrupt compositional boundary between inclusions and host magnetite (Fig. 7c) is also inconsistent with the sub-solidus exsolution process. Several studies describe that a depleted compositional halo of elements incorporated in the exsolved phase is expected around inclusions originated via exsolution-driven mechanisms (Axler and Ague, 2015; Ague and Axler, 2016; Keller and Ague, 2022). Furthermore, the presence of dolomite and intermediate members of clinochlore–chamosite solid solution is not consistent with the chemical requirement for exsolution-induced processes (see Keller and Ague, 2022), as Ca and Si are highly incompatible in magnetite and their
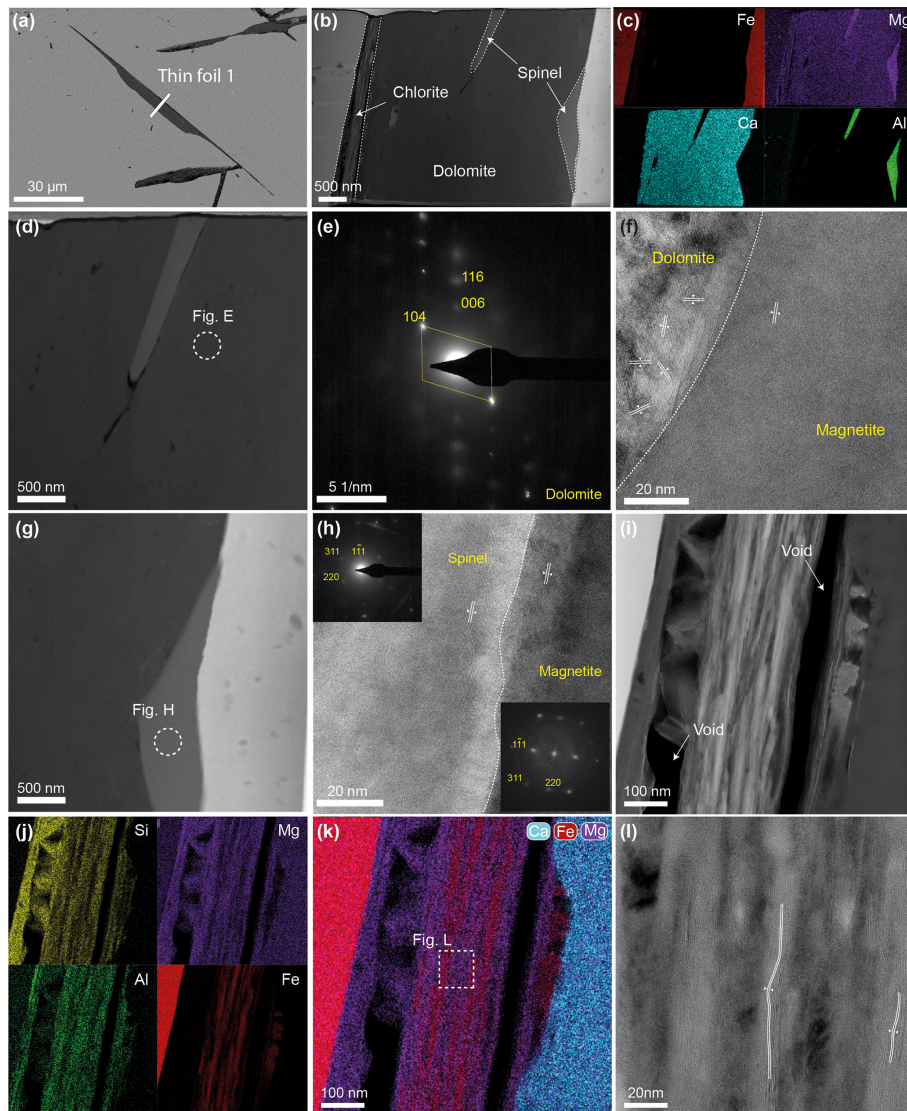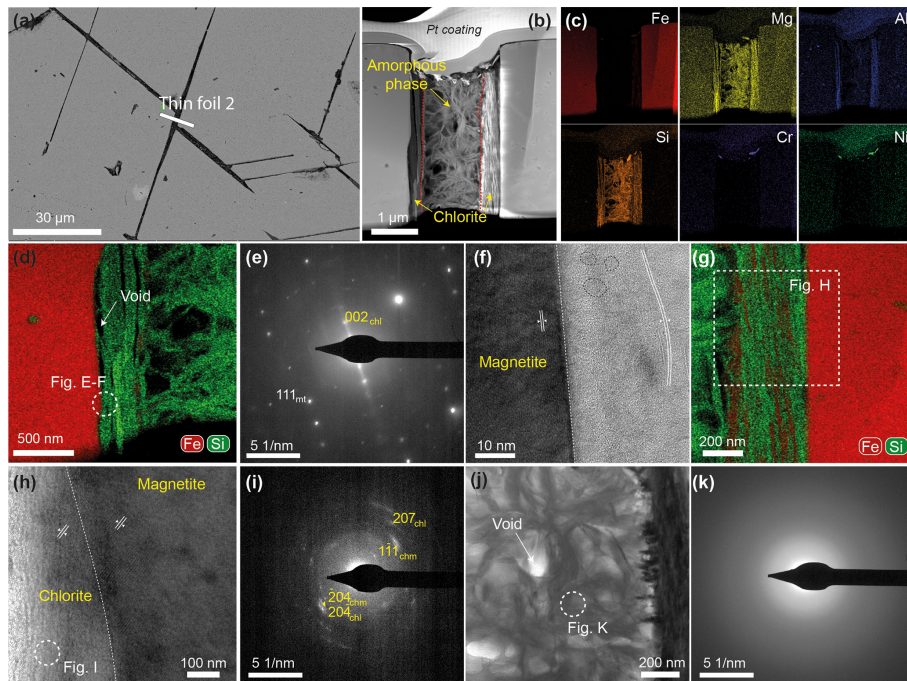
Figure 7. (a) Backscattered electron image showing the location of thin foil 1. **(b)** HAADF-STEM and **(c)** TEM–EDS maps of the thin foil. **(d)** HAADF-STEM image of the dolomite from the central part of the thin foil. **(e)** SAED image of dolomite carried out in the zone marked in **(d)**. **(f)** HRTEM image at the contact of dolomite with the magnetite host. Note the random orientation of dolomite. **(g)** HAADF-STEM image of spinel from the right part of the thin foil. **(h)** HRTEM image and corresponding FFT patterns (insets) of the contact between spinel and host magnetite in the area marked in **(g)**. **(i)** HAADF-STEM image and **(j)** TEM–EDS maps of clinochlore–chamosite from the left part of the thin foil. Note the laminar habit of crystals and the presence of voids. **(k)** Composite TEM–EDS map for Ca, Fe, and Mg of clinochlore–chamosite. Note the intergrowth of Fe- and Mg-rich crystals. The intense light-blue color represents dolomite. **(l)** HRTEM image of clinochlore–chamosite showing curved crystallographic planes.

ionic radii lie out of the "optimum radius" of $\pm 15\,\%$–$18\,\%$ radius variation (Dare et al., 2014). Spinel exhibits an epitaxial relationship with magnetite but is rotated 90° (Fig. 7h). However, Sack and Ghiorso (1991a, b) defined the existence of miscibility gaps along the $MgFe_{-1}$–$Al^2Fe_{-2}^{3+}$ exchange vector for Cr-free spinel (i.e., spinel–magnesioferrite), implying that spinel may be exsolved from Al-bearing magnesioferrite. Magnesioferrite in magnesian skarn systems is common, usually forming magnesioferrite cores surrounded by magnetite rims, indicating loss of magnesium during al-

teration (e.g., González-Pérez et al., 2022). However, EPMA reveals that magnetite in the La Víbora skarn is Fe-rich and that there is no magnesioferrite even in the cores (Supplement 1, Table S4). Therefore, we rule out the sub-solidus exsolution from magnetite as the mechanism of type 1 inclusion formation.

As mentioned above, hydrothermal fluids at the magnetite interface may reach local supersaturation under non-equilibrium conditions, driving the formation of precipitates at the magnetite boundary which are subsequently trapped

Figure 8. (a) Backscattered electron image showing the location of thin foil 2. **(b)** HAADF-STEM and **(c)** TEM–EDS maps of the thin foil. **(d)** Composite TEM–EDS map for Si and Fe of clinochlore–chamosite from the left part of the thin foil. **(e)** SAED and **(f)** HRTEM images for the contact between clinochlore–chamosite and host magnetite from the area marked in **(d)**. **(g)** Composite TEM–EDS map for Si and Fe of clinochlore–chamosite from the right part of the thin foil. Note the increase in the Fe content of the intergrowths compared to that of the left part. **(h)** HRTEM images and **(i)** SAED patterns obtained from the area marked in **(g)**. Magnetite and clinochlore–chamosite exhibit matrix matching, but the SAED pattern suggests the polycrystalline character of clinochlore–chamosite. **(j)** HAADF-STEM image of the Mg-bearing silica phase from the central part of the thin foil. **(k)** SAED pattern carried out in the area marked in **(j)** showing the amorphous character of the phase.

during magnetite growth (e.g., Deditius et al., 2018; Yin et al., 2019; Huang et al., 2022). The crystallographically controlled shapes of micro- to nano-inclusions observed in magnetite from thin foil 1 are consistent with this model (Watson, 1996; Watson et al., 2011). In this model, epitaxial relationships with host magnetite are expected as the precipitated mineral uses the magnetite crystal lattice as a template for nucleation reducing the strain energy (Yin et al., 2019). The lack of epitaxial relationships between dolomite and the magnetite host led us to rule out this hypothesis.

The mineral assemblage found in the type inclusion in magnetite is typically found in magnesian skarn systems, where dolomite represents the protolith and spinel and chlorite minerals formed during the prograde and retrograde stages, respectively, of skarn evolution (Aleksandrov, 1998). Hence, we interpret type 1 inclusions in coarse magnetite as a relic mineral association of the skarn evolution, which was trapped during the crystal growth of the inclusions' magnetite host. Mineral inclusions in magnetite have been previously associated with relics of pre-existing minerals trapped during magnetite growth (e.g., garnet and pyroxene, Tengtie Fe skarn; Zhao and Zhou, 2015).

Thin foil 2 yields a different mineral association, including intermediate members of the clinochlore–chamosite solid solution around a net-like Mg-bearing amorphous silica phase (Fig. 8). An epitaxial relationship between clinochlore–chamosite intergrowths and host magnetite along with the presence of an amorphous phase is consistent with local supersaturation of fluids under non-equilibrium conditions in the boundary layer of crystallizing magnetite, followed by entrapment during magnetite growth (Watson, 1996; Watson et al., 2011). Supersaturated conditions could explain the polycrystalline character of clinochlore–chamosite crystallites observed as well as the presence of amorphous phases shown in Fig. 8i. The marked needle-like shape of these types of nano-inclusions and their consistent orientation along the {111} of magnetite are consistent with a model of mechanical trapping of fluids during crystal growth of the magnetite host. Silicate nanoparticles in magnetite formed by local precipitation of trapped fluid inclusions have been documented in skarn, IOA, and IOCG deposits (e.g., Deditius et al., 2018; Huang and Beaudoin, 2021). Specifically, Huang et al. (2022) have documented chlorite nanoparticles with different crystal orientations within magnetite from the Alemão IOCG deposit, in Brazil, suggesting crystalliza-

tion from boundary layer supersaturated fluids under non-equilibrium conditions. The presence of hydrated phases like chlorite with crystallites showing variable lattice orientations suggests an origin related to the retrograde-stage evolution of the skarn. This hypothesis is supported by the presence of voids and the semi-coherent matrix matching between magnetite and chlorite (Fig. 8h).

The presence of an Mg-bearing amorphous silica phase in thin foil 2 is compatible with the rapid precipitation from hydrothermal fluids rich in Ca, Mg, Al, and Si during the retrograde stages of magnesian skarns (e.g., Aleksandrov, 1998). Indeed, it is common to observe late calcite, quartz, and hydrous Mg-bearing carbonate veins in skarn systems (e.g., Zhao and Zhou, 2015; González-Pérez et al., 2022, 2023). The elevated Ca and CO_2 activity during the retrograde stage of skarns (Aleksandrov, 1998) would favor the incorporation of Ca in carbonates, which is evidenced in La Víbora skarn by comb carbonate crystals filling voids in dolomitic marble (Fig. 4h–i). The hydrothermal fluids after carbonate crystallization should have been enriched in Si and, to a lesser extent, Mg, which ultimately may have formed crustiform silica in the inner parts of the voids. Crustiform textures are associated with rapid precipitation from supersaturated fluids (Moncada et al., 2012). Therefore, we made the interpretation that both chlorite and Mg-bearing amorphous silica phases most likely crystallized from fluids that became locally supersaturated at the boundary layer of growing magnetite and were subsequently trapped at the magnetite–fluid interface during mineral growth. The relatively low temperature of the system during the retrograde stage of skarn evolution does not support solid-state diffusion processes, as cation diffusion is more favorable at higher temperatures (Frost and Lindsley, 1991; Putnis, 1992, 2009).

5.2 Micro- and nano-scale inclusions track the La Víbora skarn evolutionary history

The La Víbora skarn exhibits the typical field-scale mineralogical zoning documented for magnesian skarns worldwide, including (1) forsterite, (2) diopside, and (3) periclase zones (e.g., Aleksandrov, 1998). The mineral assemblage of the gangue from these distinct zones is made of dolomite, calcite, forsterite, diopside, periclase, serpentine, chlorite, and crustiform silica, with minor amphibole. These carbonates, silicates, and oxides observed at the field scale and micro-scale match well with the micro- to nano-scale inclusions observed in magnetite and are consistent with mineral assemblages formed during both prograde and retrograde stages of magnesian skarn-forming reactions (Einaudi et al., 1981; Aleksandrov, 1998). However, some other mineral inclusions in magnetite are either absent or only observable at the micro- to nano-scale (i.e., spinel).

During the prograde stages of magnesian skarns, the common minerals formed during increasing temperature are mainly forsterite; diopside; and, in hypabyssal magnesian

skarns (i.e., up to ∼ 2 kbar), periclase; spinel is also frequently present (Aleksandrov, 1998; Meinert et al., 2005).

Forsterite is widespread in the forsterite zone as granoblastic masses with interstitial magnetite as well as non-oriented inclusions in magnetite (Figs. 4b and 5a–b). Forsterite forms during the early prograde stage of magnesian skarns by the interaction of dolomite with silica-bearing hydrothermal fluids, according to the following reaction (Aleksandrov, 1998):

$$CaMg(CO_3)_2 + 0.5H_4SiO_4 = 0.5Mg_2SiO_4 + CaCO_3$$
$$+ H_2O + C_2.$$
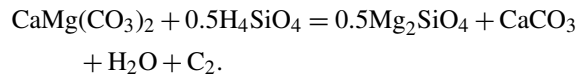
According to Einaudi et al. (1981), in the system MgO–CaO–SiO_2–CO_2–H_2O, forsterite formed at temperatures over 450–500 °C in hypabyssal magnesian skarns (< 2 kbar) (i.e., periclase is present). Interestingly, Mazzoli et al. (2013) estimated that forsterite in dolomitic marble from the Las Nieves unit originated from fluid-driven replacement reactions at ∼ 510 °C and 3 kbar. These observations suggest that magnetite formed after forsterite crystallization at temperatures above ∼ 500–510 °C. This is in accordance with the estimated minimum temperatures of magnetite formation during the prograde stage in the San Manuel skarn (i.e., < 700 °C; González-Pérez et al., 2022).

Spinel only occurs as composite nano-inclusions along with dolomite and chlorite in magnetite. Spinel is common in magnesian skarn mineral assemblages formed during the prograde stage (e.g., Einaudi et al., 1981; Meinert et al., 2005), where it is formed at increasing temperature by the interaction of hydrothermal fluids with dolomitic protoliths. To the best of our knowledge, there has been no reaction reported for spinel crystallization during the prograde stage of magnesian skarn. However, Rice (1977) proposed a reaction of chlorite and dolomite formation during the retrograde stage of skarn via the replacement of calcite according to

$$forsterite + 2\,calcite + spinel + 2CO_2 + 4H_2O$$
$$= chlorite + 2\,dolomite.$$
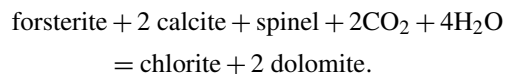
Sieber et al. (2020) modeled that the spinel stability field for the Cu–Au Ertsberg East Skarn System (EESS) was 0.51 kbar at temperatures above 550 °C for a wide range of XCO_2 and H_2O levels. Considering periclase to be an index mineral for hypabyssal skarns systems at pressures lower than 2 kbar, the value of pressure obtained by Sieber et al. (2020) fits well with that of the La Víbora skarn. According to our interpretation, inclusion type 1 was formed by entrapment of the skarn mineral assemblage during magnetite crystallization and growth. Consequently, magnetite formation should have started towards the end of the prograde stage (and likely at the incipient retrograde stage) after forsterite and likely in the conditions of the spinel stability field, that is, at temperatures above 500–550 °C. Magnetite formation during the prograde stage has been previously proposed by González-Pérez et al. (2022) for the San

Manuel magnesian skarn (southern Spain) as well as by Zhao and Zhou (2015) for the Tengtie skarn (southern China). On the other hand, the growth of magnetite likely occurred during the retrograde stage, as evidenced by the presence of an amorphous phase formed during the cooling of saturated hydrothermal fluid at the magnetite boundary, as well as the epitaxial nucleation and growth of chlorite on the magnetite host. According to Sieber et al. (2020), chlorite forms at temperatures below 550 °C, whereas geothermometry calculations carried out by González-Pérez et al. (2022) in the San Manuel skarn obtained a temperature of 267–435 °C, which overlaps decreasing temperatures during the retrograde skarn stage (Aleksandrov, 1998). On the other hand, the solubility of various forms of silica in water (amorphous silica, opal, cristobalite, chalcedony, and quartz) increases with temperatures in the range of 10 to 100 ppm for temperatures of < 50–100 °C and up to 1000 ppm above 300 °C; thereafter, the solubility of silica decreases (Fournier, 1985). Silica supersaturation promotes precipitation of amorphous (opaline) silica at temperatures of approximately 140 °C. Amorphous silica is unstable and with time forms chalcedony or fine-grained quartz. These facts suggest that magnetite growth occurred during the retrograde stage of skarn evolution at a decreasing temperature from approximately below 550 °C. Subsequent growth of magnetite may have continued down to the late retrograde stage of skarn evolution.

6 Conclusions

EPMA and TEM studies reveal that La Víbora magnetite hosts micro-scale forsterite inclusions as well as variably oriented nano-inclusions along the {111} of magnetite. Type 1 composite nano-inclusions include spinel, dolomite, and intermediate members of the clinochlore–chamosite solid solution interpreted as relicts of prograde skarn reactions trapped as a solid inclusion during magnetite growth. Type 2 composite nano-inclusions include intermediate members of the clinochlore–chamosite solid solution as well as the Mg-bearing amorphous silica phase. Its formation is ascribed to the local supersaturation of hydrothermal fluids at the magnetite boundary under non-equilibrium conditions followed by entrapment during magnetite growth during the retrograde skarn stage.

Non-oriented inclusions of forsterite and type 1 nano-inclusions in magnetite track magnetite crystallization during the prograde stage of the skarn evolution at temperatures > 510 °C. The oriented type 2 nano-inclusions belong to hydrated phases formed from supersaturated fluids at the magnetite boundary during the retrograde stage of the skarn at temperatures below approximately 500 °C. Growth of magnetite during the retrograde stage of skarn evolution led to fluid entrapment at the magnetite boundary layer. Such fluids became supersaturated and crystallized mainly clinochlore–

chamosite intergrowths and Mg-bearing amorphous silica phases during decreasing temperatures of retrograde skarn.

This constrains the time of the beginning of magnetite formation during the prograde stage of the La Víbora skarn and its continuing growth during the retrograde stage of the skarn. Thus, magnetite from the La Víbora skarn provides an excellent example for the study of mineral formation during magnetite growth. Moreover, nano-scale mineral assemblages can be used to constrain the timing of the magnetite formation during skarn evolution.

References

Acosta-Vigil, A., Rubatto, D., and Bartoli, O.: Age of anatexis in the crustal footwall of the Ronda peridotites, S Spain, Lithos, 210–211, 147–167, https://doi.org/10.1016/j.lithos.2014.08.018, 2014.

Ague, J. J. and Axler, J. A.: Interface coupled dissolution-reprecipitation in garnet from subducted granulites and ultrahigh-pressure rocks revealed by phosphorous, sodium, and titanium zonation, Am. Mineral., 101, 1696–1699, https://doi.org/10.2138/am-2016-5707, 2016.

Aleksandrov, S. M. (Ed.): Geochemistry of skarn and ore formation in dolomites, VSP, Utrecht, the Netherlands, 142 pp., ISBN 9067642819, 1998.

Axler, J. A. and Ague, J. J.: Oriented multiphase needles in garnet from ultrahigh-temperature granulites, Connecticut, USA, Am. Mineral., 100, 2254–2271, https://doi.org/10.2138/am-2015-5018, 2015.

Balanyá, J. C., García-Dueñas, V., Azañón, J. M., and Sánchez-Gómez, M.: Alternating contractional and extensional events in the Alpujarride nappes of the Alboran Domain (Betics, Gibraltar Arc), Tectonics, 16, 226–238, https://doi.org/10.1029/96TC03871, 1997.

Barich, A., Acosta-Vigil, A., Garrido, C. J., Cesare, B., Tajčmanová, L., and Bartoli, O.: Microstructures and petrology of melt inclusions in the anatectic sequence of Jubrique (Betic Cordillera, S Spain): Implications for crustal anatexis, Lithos, 206–207, 303–320, 2014.

Bosi, F., Hålenius, U., and Skogby, H.: Crystal chemistry of the magnetite-ulvospinel series, Am. Mineral., 94, 181–189, https://doi.org/10.2138/am.2009.3002, 2009.

Brown, B. T. and Bailey, S. W.: Chlorite polytypism: I. Regular and semi-random one-layer structures, Am. Mineral., 47, 819–850, 1962.

Canil, D. and Lacourse, T.: Geothermometry using minor and trace elements in igneous and hydrothermal magnetite, Chem. Geol., 541, 119576, https://doi.org/10.1016/j.chemgeo.2020.119576, 2020.

Calvo, G., Rodríguez, O., Serrano Guevara, M. V., Tornos, F., Rodríguez Mejía, R., Velasco Roldán, F., Contreras, M., Ochoa, J., Milena, U., and Sapacayo, M.: El skarn magnésico de Pampa del Pongo: Un megayacimiento de hierro en la Cordillera de la Costa del sur del Perú, Bol. Soc. Geol. Perú, 107, 99–103, 2013.

Cepedal, A., Martìn-Izard, A., Reguilón, R., Rodrìguez-Pevida, L., Spiering, E., and González-Nistal, S.: Origin and evolution of the calcic and magnesian skarns hosting the El Valle-Boinás copper-gold deposit, Asturias (Spain), J. Geochem. Explor., 71, 119–151, https://doi.org/10.1016/S0375-6742(00)00149-7, 2000.

Chang, Z., Shu, Q., and Meinert, L.: Chapter 6: Skarn deposits of China, in: Special Publications of Society of Economic Geology, edited by: Chang, Z. and Goldfarb, R. J., China, 22, ISBN 9781629493107, 2019.

Chen, F., Deng, J., Wang, Q., Huizenga, J. M., Li, G., and Gu, Y.: LA-ICP-MS trace element analysis of magnetite and pyrite from

the Hetaoping Fe-Zn-Pb skarn deposit in Baoshan block, SW China: Implications for ore-forming processes, Ore Geol. Rev., 117, 103309, https://doi.org/10.1016/j.oregeorev.2020.103309, 2020.

Ciobanu, C. L., Verdugo-Ihl, M. R., Slattery, A., Cook, N. J., Ehrig, K., Courtney-Davies, L., and Wade, B. P.: Silician magnetite: Si–Fe-nanoprecipitates and other mineral inclusions in magnetite from the Olympic Dam Deposit, South Australia, Minerals, 9, 311, https://doi.org/10.3390/min9050311, 2019.

Cuevas, J., Esteban, J. J., and Tubía, J. M.: Tectonic implications of the granite dyke swarm in the Ronda peridotites (Betic Cordilleras, Southern Spain), J. Geol. Soc. London, 163, 631–640, https://doi.org/10.1144/0016-764905-038, 2006.

Dare, S. A., Barnes, S. J., Beaudoin, G., Méric, J., Boutroy, E., and Potvin-Doucet, C.: Trace elements in magnetite as petrogenetic indicators, Miner. Deposita, 49, 785–796, https://doi.org/10.1007/s00126-014-0529-0, 2014.

Deditius, A. P., Reich, M., Simon, A. C., Suvorova, A., Knipping, J., Roberts, M. P., Rubanov, S., Dood, A., and Saunder, M.: Nanogeochemistry of hydrothermal magnetite, Contrib. Mineral. Petr., 173, 1–20, https://doi.org/10.1007/s00410-018-1474-1, 2018.

Díaz-Alvarado, J., González-Menéndez, L., Hidas, K., Azor, A., and Pedrera, A.: Tectono-metamorphic interaction of upper mantle peridotites and lower crustal units during continental rifting in the western Betic Cordillera, Gondwana Res., 132, 193–219, https://doi.org/10.1016/j.gr.2024.03.018, 2024.

Dropp, G.: A general equation for estimating Fe_3 concentrations in ferromagnesian silicates and oxides from microprobe analyses, using stoichiometric criteria, Mineral. Mag., 51, 431–435, https://doi.org/10.1180/minmag.1987.051.361.10, 1987.

Dupuis, C. and Beaudoin, G.: Discriminant diagrams for iron oxide trace element fingerprinting of mineral deposit types, Mineral. Deposita, 46, 319–335, https://doi.org/10.1007/s00126-011-0334-y, 2011.

Egeler, C. G. and Simon, O. J.: Orogenic evolution of the Betic Zone (Betic Cordilleras, Spain), with emphasis on the nappe structures, Geol. Mijnbouw, 48, 296–305, 1969.

Einaudi, M. T., Meinert, L. D., and Newberry, R. J.: Skarn deposits, in: SEG Economic Geology 75th Anniversary Volume, edited by: Skinner, J. B., Economic Geology Publishing Company, 317–339, https://doi.org/10.5382/AV75.11, 1981.

Esteban, J. J., Sánchez-Rodríguez, L., Seward, D., Cuevas, J., and Tubía, J. M.: The late thermal history of the Ronda area, southern Spain, Tectonophysics, 389, 81–92, https://doi.org/10.1016/j.tecto.2004.07.050, 2004.

Esteban, J. J., Cuevas, J., Tubía, J. M., Liati, A., Seward, D., and Gebauer, D.: Timing and origin of zircon-bearing chlorite schists in the Ronda peridotites (Betic Cordilleras, Southern Spain), Lithos, 99, 121–135, https://doi.org/10.1016/j.lithos.2007.06.006, 2007.

Esteban, J. J., Cuevas, J., Vegas, N., and Tubía, J. M.: Deformation and kinematics in a melt-bearing shear zone from the Western Betic Cordilleras (Southern Spain), J. Struct. Geol., 30, 380–393, https://doi.org/10.1016/j.jsg.2007.11.010, 2008.

Esteban, J. J., Cuevas, J., Tubía, J. M., Sergeev, S., and Larionov, A.: A revised Aquitanian age for the emplacement of the Ronda peridotites (Betic Cordilleras, southern Spain), Geol. Mag., 148, 183–187, https://doi.org/10.1017/S0016756810000737, 2010.

Falini, G., Foresti, E., Gazzano, M., Gualtieri, A. F., Leoni, M., Lesci, I. G., and Roveri, N.: Tubular-shaped stoichiometric chrysotile nanocrystals, Chem.-Eur. J., 10, 3043–3049, 2004.

Fitros, M., Tombros, S. F., Kokkalas, S., Kilias, S. P., Perraki, M., Skliros, V., Simon, X. C., Papaspyropoulos, K., Avgouropoulos, G., Williams-Jones, A. E., Zhai, D., and Hatzipanagiotou, K.: REE-enriched skarns in collisional settings: The example of Xanthi's Fe-skarn, Rhodope Metallogenetic Massif, Northern Greece, Lithos, 370, 105638, https://doi.org/10.1016/j.lithos.2020.105638, 2020.

Fournier, R. O.: The behavior of silica in hydrothermal solutions, in: Geology and Geochemistry of Epithermal Systems, edited by: Berger, B. R. and Bethke, P. M., Rev. Econ. Geol., 2, https://doi.org/10.5382/Rev.02.03, 1985.

Frost, B. R. and Lindsley, D. H.: Occurrence of iron-titanium oxides in igneous rocks, Rev. Mineral. Geochem., 25, 433–468, 1991.

Garrido, C. J. and Bodinier, J.-L.: Diversity of Mafic Rocks in the Ronda Peridotite: Evidence for Pervasive Melt–Rock Reaction during Heating of Subcontinental Lithosphere by Upwelling Asthenosphere, J. Petrol., 40, 729–754, https://doi.org/10.1093/petroj/40.5.729, 1999.

Garrido, C. J., Gueydan, F., Booth-Rea, G., Precigout, J., Hidas, K., Padron-Navarta, J. A., and Marchesi, C.: Garnet lherzolite and garnet-spinel mylonite in the Ronda peridotite: Vestiges of Oligocene backarc mantle lithospheric extension in the western Mediterranean, Geology, 39, 927–930, https://doi.org/10.1130/G31760.1, 2011.

Gervilla, F., González-Jiménez, J.M., Hidas, K., Marchesi, C., and Piña, R. (Eds.): Geology and metallogeny of the upper mantle rocks from the Serranía de Ronda, Monography of the Spanish Mineralogical Society, 122 pp., ISBN 9878415588306, 2019.

Goldsmith, J. R., Graf, D. L., and Heard, H. C.: Lattice constants of the calcium magnesium carbonates, Am. Mineral., 46, 453–459, 1961.

González-Jiménez, J. M., Villaseca, C., Griffin, W. L., Belousova, E. A., Konc, Z., Ancochea, E., O'Reilly, S. Y., Pearson, N. J., Garrido, C. J., and Gervilla, F.: The architecture of the European-Mediterranean lithosphere: A synthesis of the Re-Os evidence, Geology, 41, 547–550, https://doi.org/10.1130/G34003.1, 2013a.

González-Jiménez, J. M., Marchesi, C., Griffin, W. L., Gutiérrez-Narbona, R., Lorand, J.-P., O'Reilly, S. Y., Garrido, C. J., Gervilla, F., Pearson, N. J., and Hidas, K.: Transfer of Os isotopic signatures from peridotite to chromitite in the subcontinental mantle: Insights from in situ analysis of platinum-group and base-metal minerals (Ojén peridotite massif, southern Spain), Lithos, 164–167, 74–85, https://doi.org/10.1016/j.lithos.2012.07.009, 2013b.

González-Jiménez, J. M., Marchesi, C., Griffin, W. L., Gervilla, F., Belousova, E. A., Garrido, C. J., Romero, R., Talavera, C., Leisen, M., O'Reilly, S. Y., Barra, F., and Martin, L.: Zircon recycling and crystallization during formation of chromite- and Ni-arsenide ores in the subcontinental lithospheric mantle (Serranía de Ronda, Spain), Ore Geol. Rev., 90, 193–209, https://doi.org/10.1016/j.oregeorev.2017.02.012, 2017.

Gonzalez-Perez, I., González-Jiménez, J. M., Gervilla, F., Fanlo, I., Tornos, F., Colás, V., Arranz, E., Hanchar, J., Abad-Ortega, M. D. M, Moreno-Abril, A. J., Carrión, M., and Noval, S.: Genesis and evolution of the San Manuel iron skarn deposit (Betic Cordillera, SW Spain), Ore Geol. Rev., 141, 104657, https://doi.org/10.1016/j.oregeorev.2021.104657, 2022.

González-Pérez, I., Fanlo, I., Ares, G., Gervilla, F., González-Jiménez, J. M., Acosta-Vigil, A., and Arranz, E.: The Unconventional Peridotite-Related Mg-Fe-B Skarn of the El Robledal, SE Spain, Minerals, 13, 300, https://doi.org/10.3390/min13030300, 2023.

Guo, X., Zhou, T., Wang, F., Fan, Y., Fu, P., and Kong, F.: Distribution of Co, Se, Cd, In, Re and other critical metals in sulfide ores from a porphyry-skarn system: A case study of Chengmenshan Cu deposit, Jiangxi, China, Ore Geol. Rev., 158, 105520, https://doi.org/10.1016/j.oregeorev.2023.105520, 2023.

Hidas, K., Booth-Rea, G., Garrido, C. J., Martínez-Martínez, J. M., Padrón-Navarta, J. A., Konc, Z., Giaconia, F., Frets, E., and Marchesi, C.: Backarc basin inversion and subcontinental mantle emplacement in the crust: kilometer-scale folding and shearing at the base of the proto-Alborán lithospheric mantle (Betic Cordillera, southern Spain), J. Geol. Soc. London, 170, 47–55, https://doi.org/10.1144/jgs2011-151, 2013.

Hidas, K., Varas-Reus, M. I., Garrido, C. J., Marchesi, C., Acosta-Vigil, A., Padrón-Navarta, J. A., Targuisti, K., and Konc, Z.: Hyperextension of continental to oceanic-like lithosphere: The record of late gabbros in the shallow subcontinental lithospheric mantle of the westernmost Mediterranean, Tectonophysics, 650, 65–79, https://doi.org/10.1016/j.tecto.2015.03.011, 2015.

Hu, H., Lentz, D., Li, J.-W., McCarron, T., Zhao, X. F., and Hall, D.: Reequilibration processes in magnetite from iron skarn deposits, Econ. Geol., 110, 1–8, https://doi.org/10.2113/econgeo.110.1.1, 2015.

Huang, X. W. and Beaudoin, G.: Textures and chemical compositions of magnetite from iron oxide copper-gold (IOCG) and Kiruna-type iron oxide-apatite (IOA) deposits and their implications for ore genesis and magnetite classification schemes, Econ. Geol., 114, 953–979, https://doi.org/10.5382/econgeo.4651, 2019.

Huang, X. W. and Beaudoin, G.: Nanoinclusions in zoned magnetite from the Sossego IOCG deposit, Carajás, Brazil: Implication for mineral zoning and magnetite origin discrimination, Ore Geol. Rev., 139, 104453, https://doi.org/10.1016/j.oregeorev.2021.104453, 2021.

Huang, X. W., Boutroy, E., Makvandi, S., Beaudoin, G., Corriveau, L., and De Toni, A. F.: Trace element composition of iron oxides from IOCG and IOA deposits: Relationship to hydrothermal alteration and deposit subtypes, Miner. Deposita, 54, 525–552, https://doi.org/10.1007/s00126-018-0825-1, 2019.

Huang, X. W., Beaudoin, G., and Yang, Y.: A HR-TEM study on two generations of magnetite from the Alemao IOCG deposit, Carajás, Brazil: Implication for Fe-Cu mineralization, Ore Geol Rev., 146, 104934, https://doi.org/10.1016/j.oregeorev.2022.104934, 2022.

Ivanyuk, G. Y., Kalashnikov, A. O., Pakhomovsky, Y. A., Bazai, A. V., Goryainov, P. M., Mikhailova, J. A., Yakovenchuk, V. N., and Konopleva, N. G.: Subsolidus evolution of the magnetite-spinel-ulvöspinel solid solutions in the Kovdor phosphorite-carbonatite complex, NW Russia, Minerals, 7, 215, https://doi.org/10.3390/min7110215, 2017.

Jansson, N. F. and Allen, R. L.: Multistage ore formation at the Ryllshyttan marble and skarn-hosted Zn–Pb–Ag–(Cu) magnetite

deposit, Bergslagen, Sweden, Ore Geol. Rev., 69, 217–242, https://doi.org/10.1016/j.oregeorev.2015.02.018, 2015.

Keller, D. S. and Ague, J. J.: Predicting and explaining crystallographic orientation relationships of exsolved precipitates in garnet using the edge-to-edge matching model, J. Metamorph. Geol., 40, 1189-1218, https://doi.org/10.1111/jmg.12662, 2022.

Knipping, J. L., Bilenker, L. D., Simon, A. C., Reich, M., Barra, F., Deditius, A. P., Wälle, M., Heinrich, C. A., Holtz, F., and Munizaga, R.: Trace elements in magnetite from massive iron oxide-apatite deposits indicate a combined formation by igneous and magmatic-hydrothermal processes, Geochim. Cosmochim. Ac., 171, 15–38, https://doi.org/10.1016/j.gca.2015.08.010, 2015.

Kuşcu, İ.: Skarns and Skarn Deposits of Turkey, in: Mineral Resources of Turkey, edited by: Pirajno, F., Ünlü, T., Dönmez, C., and Şahin, M., Modern Approaches in Solid Earth Sciences, 16, Springer, Cham, https://doi.org/10.1007/978-3-030-02950-0_7, 2019.

Lefebvre, M. G., Romer, R. L., Glodny, J., and Roscher, M.: Skarn formation and tin enrichment during regional metamorphism: the Hämmerlein polymetallic skarn deposit, Lithos, 348, 105171, https://doi.org/10.1016/j.lithos.2019.105171, 2019.

Lister, J. S. and Bailey, S. W.: Chlorite polytypism: IV. Regular two-layer structures, Am. Mineral., 52, 1614–1631, 1967.

Mao, J., Zhou, Y., Liu, H., Zhang, C., Fu, D., and Liu, B.: Metallogenic setting and ore genetic model for the Beiya porphyry-skarn polymetallic Au orefield, western Yunnan, China, Ore Geol. Rev., 86, 21–34, https://doi.org/10.1016/j.oregeorev.2017.02.003, 2017.

Marchesi, C., Griffin, W. L., Garrido, C. J., Bodinier, J. L., O'Reilly, S. Y., and Pearson, N. J.: Persistence of mantle lithospheric Re-Os signature during asthenospherization of the subcontinental lithospheric mantle: insights from in situ isotopic analysis of sulfides from the Ronda peridotite (Southern Spain), Contrib. Mineral. Petr., 159, 315–330, https://doi.org/10.1007/s00410-009-0429-y, 2010.

Marchesi, C., Garrido, C. J., Bosch, D., Bodinier J.L., Hidas, K., Padrón-Navarta, J. A., and Gervilla, F.: A Late Oligocene supra-subduction setting in the westernmost Mediterranean revealed by intrusive pyroxenite dikes in the Ronda peridotite (southern Spain), J. Geol., 120, 237–247, https://doi.org/10.1086/663875, 2012.

Marincea, S. and Dumitraş, D-G.: Contrasting types of boron-bearing deposits in magnesian skarns from Romania, Ore Geol. Rev., 112, 102952, https://doi.org/10.1016/j.oregeorev.2019.102952, 2019.

Mazzoli, S. and Algarra, A. M.: Deformation partitioning during transpressional emplacement of a "mantle extrusion wedge": the Ronda peridotites, western Betic Cordillera, Spain, J. Geol. Soc. London, 168, 373–382, https://doi.org/10.1144/0016-76492010-126, 2011.

Mazzoli, S., Martín-Algarra, A., Reddy, S. M., Sánchez-Vizcaíno, V. L., Fedele, L., and Noviello, A.: The evolution of the footwall to the Ronda subcontinental mantle peridotites: insights from the Nieves Unit (western Betic Cordillera), J. Geol. Soc. London, 170, 385–402, https://doi.org/10.1144/jgs2012-105, 2013.

Meinert, L. D., Dipple, G. M., and Nicolescu, S.: World skarn deposits, Society of Economic Geologists, https://doi.org/10.5382/AV100.11, 2005.

Mellini, M.: The crystal structure of lizardite 1 T: hydrogen bonds and polytypism, Am. Mineral., 67, 587–598, 1982.

Moncada, D., Mutchler, S., Nieto, A., Reynolds, T. J., Rimstidt, J. D., and Bodnar, R. J.: Mineral textures and fluid inclusion petrography of the epithermal Ag-Au deposits at Guanajuato, Mexico: Application to exploration, J. Geochem. Explor., 114, 20–35, https://doi.org/10.1016/j.gexplo.2011.12.001, 2012.

Nadoll, P., Angerer, T., Mauk, J. L., French, D., and Walshe, J.: The chemistry of hydrothermal magnetite: A review, Ore Geol Rev., 61, 1–32, https://doi.org/10.1016/j.oregeorev.2013.12.013, 2014.

Nakagiri, N., Manghnani, M. H., Ming, L. C., and Kimura, S.: Crystal structure of magnetite under pressure, Phys. Chem. Miner., 13, 238–244, 1986.

Navarro-Vilá, F. and Tubía, J. M.: Essai d'une nouvelle differentiation des Nappes Alpujarrides dans le secteur occidental des Cordillères Bétiques (Andalousie, Espagne), CR Académie des Sciences, Paris, 296 (série II), 111–114, 1983.

Obata, M.: The Ronda peridotite-garnet-lherzolite, spinel-lherzolite, and plagioclase-lherzolite facies and the PT trajectories of a high-temperature mantle Intrusion, J. Petrol., 21, 533–572, 1980.

O'Hanley, D. S. and Dyar, M. D.: The composition of lizardite 1T and the formation of magnetite in serpentinites, Am. Mineral., 78, 391-404, 1993.

Peterson, R. C., Lager, G. A., and Hitterman, R. L.: A time-of-flight neutron powder diffraction study of $MgAl_2O_4$ at temperatures up to 1273 K, Am. Mineral., 76, 1455–1458, 1991.

Platt, J. P., Behr, W. M., Johanesen, K., and Williams, J. R.: The Betic-Rif arc and its orogenic hinterland: a review, Annu. Rev. Earth. Pl. Sc., 41, 313–357, https://doi.org/10.1146/annurev-earth-050212-123951, 2013.

Pouchou, J. L. and Pichoir, F.: Quantitative analysis of homogeneous or stratified microvolumes applying the model "PAP", in: Electron probe quantitation, edited by: Heinrich, K. F. J. and Newbury, D. E., Springer, Boston, MA, 31–75, https://doi.org/10.1007/978-1-4899-2617-3_4, 1991.

Pouchou, J. L. and Pichoir, F.: Electron probe X-ray microanalysis applied to thin surface films and stratified specimens, Scanning Microscopy, 7, 12, 1993.

Precigout, J., Gueydan, F., Gapais, D., Garrido, C. J., and Essaifi, A.: Strain localisation in the subcontinental mantle — a ductile alternative to the brittle mantle, Tectonophysics, 445, 318–336, https://doi.org/10.1016/j.tecto.2007.09.002, 2007.

Putnis, A.: An introduction to mineral sciences, Cambridge University Press, ISBN: 9781139170383, 1992.

Putnis, A.: Mineral replacement reactions: from macroscopic observations to microscopic mechanisms, Mineral. Mag., 66, 689–708, 2002.

Putnis, A.: Mineral replacement reactions, Rev. Miner. Geochem., 70, 87–124, https://doi.org/10.2138/rmg.2009.70.3, 2009.

Reisberg, L. and Lorand, J. P.: Longevity of sub-continental mantle lithosphere from osmium isotope systematics in orogenic peridotite massifs, Nature, 376, 159–162, https://doi.org/10.1038/376159a0, 1995.

Rice, J. M.: Contact metamorphism of impure dolomitic limestone in the Boulder aureole, Montana, Contrib, Mineral. Petr., 59, 237–259, 1977.

Sánchez-Navas, A., Martín-Algarra, A., Blanco-Quintero, I., and Garcia-Casco, A.: Pre-Alpine prograde evolu-

tion of the Upper Alpujarride (Betic-Rif belt) reveals a Paleotethys-related collision, Int. Geol. Rev., 66, 405–438, https://doi.org/10.1080/00206814.2023.2246546, 2024.

Sánchez-Rodríguez, L. and Gebauer, D.: Mesozoic formation of pyroxenites and gabbros in the Ronda area (southern Spain), followed by Early Miocene subduction metamorphism and emplacement into the middle crust: U–Pb sensitive high-resolution ion microprobe dating of zircon, Tectonophysics, 316, 19–44, https://doi.org/10.1016/S0040-1951(99)00256-5, 2000.

Sanz de Galdeano, C.: Discussion on the differentiation of tectonic units in the Alpujarride Complex (Betic Cordillera), Estudios Geológicos, 79, e151, https://doi.org/10.3989/egeol.44907.627, 2023.

Sanz de Galdeano, C. and Ruiz Cruz, M. D.: Late Palaeozoic to Triassic formations unconformably deposited over the Ronda peridotites (Betic Cordilleras): Evidence for their Variscan time of crustal emplacement, Estudios Geológicos, 72, e043, https://doi.org/10.3989/egeol.42046.368, 2016.

Sack, R. O. and Ghiorso, M. S.: Chromian spinel as petrogenetic indicators: thermodynamics and petrological applications, Am. Mineral., 76, 827–847, 1991a.

Sack, R. O. and Ghiorso, M. S.: An internally consistent model for the thermodynamic properties of Fe-Mg-titanomagnetite-aluminate spinels, Contrib. Mineral. Petr., 106, 474–505, 1991b.

Sieber, M. J., Brink, F. J., Leys, C., King, P. L., and Henley, R. W.: Prograde and retrograde metasomatic reactions in mineralised magnesium-silicate skarn in the Cu-Au Ertsberg East Skarn System, Ertsberg, Papua Province, Indonesia, Ore Geol. Rev., 125, 103697, https://doi.org/10.1016/j.oregeorev.2020.103697, 2020.

Soloviev, S. G., Kryazhev, S. G., Dvurechenskaya, S. S., Kryazhev, V. S., Emkuzhev, M. S., and Bortnikov, N. S.: The superlarge Tyrnyauz skarn W-Mo and stockwork Mo (-W) to Au (-Mo, W, Bi, Te) deposit in the Northern Caucasus, Russia: Geology, geochemistry, mineralization, and fluid inclusion characteristics, Ore Geol. Rev., 138, 104384, https://doi.org/10.1016/j.oregeorev.2021.104384, 2021.

Tan, W., Liu, P., He, H., Wang, C. Y., and Liang, X.: Mineralogy and origin of exsolution in Ti-rich magnetite from different magmatic Fe-Ti oxide-bearing intrusions, Can. Mineral., 54, 539–553, https://doi.org/10.3749/canmin.1400069, 2016.

Tubía, J. M. and Cuevas, J.: High-temperature emplacement of the Los Reales peridotite nappe (Betic Cordillera, Spain), J. Struct. Geol., 8, 473–482, https://doi.org/10.1016/0191-8141(86)90064-7, 1986.

Tubía, J. M., Cuevas, J. M., and Ibarguchi, J. I. G.: Sequential development of the metamorphic aureole beneath the Ronda peridotites and its bearing on the tectonic evolution of the Betic Cordillera, Tectonophysics, 279, 227–252, https://doi.org/10.1016/S0040-1951(97)00124-8, 1997.

Tubía, J. M., Cuevas, J., and Esteban, J. J.: Localization of deformation and kinematic shift during the hot emplacement of the Ronda peridotites (Betic Cordilleras, southern Spain), J. Struct. Geol., 50, 148–160, https://doi.org/10.1016/j.jsg.2012.06.010, 2013.

Van der Wal, D. and Vissers, R. L. M.: Uplift and emplacement of upper mantle rocks in the western Mediterranean, Geology, 21, 1119–1122, https://doi.org/10.1130/0091-7613(1993)021<1119:UAEOUM>2.3.CO;2, 1993.

Van der Wal, D. and Vissers, R. L. M.: Structural Petrology of the Ronda Peridotite, SW Spain: Deformation History, J. Petrol, 37, 23–43, https://doi.org/10.1093/petrology/37.1.23, 1996.

Vissers, R. L. M., Platt, J. P., and Van der Wal, D.: Late orogenic extension of the Betic Cordillera and the Alboran Domain: A lithospheric view, Tectonics, 14, 786–803, https://doi.org/10.1029/95TC00086, 1995.

Walker, J. R. and Bish, D. L.: Application of Rietveld refinement techniques to a disordered II b Mg-chamosite, Clay. Clay Miner., 40, 319–322, 1992.

Watson, E. B.: Surface enrichment and trace-element uptake during crystal growth, Geochim. Cosmochim. Ac., 60, 5013–5020, https://doi.org/10.1016/S0016-7037(96)00299-2, 1996.

Watson, E. B., Lanzillo, N. A., and Nayak, S. K.: The Growth Entrapment Model (GEM): New Insights from Molecular-Scale Simulations of Ti in Quartz, in: AGU Fall Meeting Abstracts, San Francisco, California, 5–9 December 2011, PP51E-04, 2011.

Xie, G. Q., Mao, J. W., Richards, J. P., Han, Y. X., and Fu, B.: Distal Au deposits associated with Cu–Au skarn mineralization in the Fengshan area, eastern China, Econ. Geol., 114, 127–142, https://doi.org/10.5382/econgeo.2019.4623, 2019.

Xie, Q. H., Zhang, Z. C., Jin, Z. L., Santosh, M., Liu, H., Wang, K. Y., Zhao, P. L., and He, H. H.: The high-grade Fe skarn deposit of Jinling, North China Craton: insights into hydrothermal iron mineralization, Ore Geol. Rev., 138, 104395, https://doi.org/10.1016/j.oregeorev.2021.104395, 2021.

Yin, S., Wirth, R., Ma, C., and Xu, J.: The role of mineral nanoparticles at a fluid-magnetite interface: Implications for trace-element uptake in hydrothermal systems, Am. Mineral., 104, 1180–1188, https://doi.org/10.2138/am-2019-6996, 2019.

Yund, R. A. and McCallister, R. H.: Kinetics and mechanisms of exsolution, Chem. Geol., 6, 5–30, https://doi.org/10.1016/0009-2541(70)90002-1, 1970.

Zhang, Z., Du, Y., and Zhang, J.: Alteration, mineralization, and genesis of the zoned Tongshan skarn-type copper deposit, Anhui, China, Ore Geol. Rev., 53, 489–503, https://doi.org/10.1016/j.oregeorev.2013.02.009, 2013.

Zhang, Z. C., Hou, T., Santosh, M., Li, H. M., Li, J. W., Zhang, Z. H., Song, X. Y., and Wang, M.: Spatio-temporal distribution and tectonic settings of the major iron deposits in China, An overview, Ore Geol Rev., 57, 247–263, https://doi.org/10.1016/j.oregeorev.2013.08.021, 2014.

Zhao, W. W. and Zhou, M. F.: In-situ LA–ICP-MS trace elemental analyses of magnetite: The Mesozoic Tengtie skarn Fe deposit in the Nanling Range, South China, Ore Geol Rev., 65, 872–883, https://doi.org/10.1016/j.oregeorev.2014.09.019, 2015.

Zhao, W. W., Zhou, M.-F., Li, Y. H. M., Zhao, Z., and Gao, J.-F.: Genetic types, mineralization styles, and geodynamic settings of Mesozoic tungsten deposits in South China, J. Asian Earth Sci., 137, 109–140, https://doi.org/10.1016/j.jseaes.2016.12.047, 2017.

Zheng, H., Chen, H., Wu, C., Jiang, H., Gao, C., Kang, Q., Yang, C., Wang, D., and Lai, C.-K.: Genesis of the supergiant Huayangchuan carbonatite-hosted uranium-polymetallic deposit in the Qinling Orogen, Central China, Gondwana Res., 86, 250–265, https://doi.org/10.1016/j.gr.2020.05.016, 2020.